LETTER • OPEN ACCESS

Broadening of microwave heating beams in the DIII-D tokamak by edge turbulence

OPEN ACCESS
IOP Publishing | International Atomic Energy Agency
Nuclear Fusion
Nucl. Fusion **63** (2023) 044001 (7pp)
https://doi.org/10.1088/1741-4326/acbb8e

Letter

Broadening of microwave heating beams in the DIII-D tokamak by edge turbulence

M.W. Brookman[1,2], L.A. Holland[3], M.B. Thomas[3], M.E. Austin[1], K. Barada[4], K.W. Gentle[1], R.J. La Haye[5], J.B. Leddy[3], C.C. Petty[5], T.L. Rhodes[4], Z. Yan[6], R.G.L. Vann[3] and A. Köhn-Seemann[7,*]

[1] Institute for Fusion Studies, University of Texas at Austin, Austin, TX 78712, United States of America
[2] Commonwealth Fusion Systems, 117 Hospital Rd, Devens, MA 01434, United States of America
[3] York Plasma Institute, Department of Physics, University of York, Heslington, York YO10 5DD, United Kingdom of Great Britain and Northern Ireland
[4] Department of Physics and Astronomy, University of California Los Angeles, Los Angeles, CA 90095, United States of America
[5] General Atomics, PO Box 85608, San Diego, CA 92186, United States of America
[6] University of Wisconsin-Madison, Madison, WI 53706, United States of America
[7] Institute of Interfacial Process Engineering and Plasma Technology, University of Stuttgart, Stuttgart, Germany

E-mail: koehn@igvp.uni-stuttgart.de

Received 28 July 2022, revised 25 January 2023
Accepted for publication 13 February 2023
Published 1 March 2023

Abstract

We have demonstrated for the first time that turbulent plasma density fluctuations in the edge of the DIII-D tokamak are responsible for substantial broadening of an injected microwave beam by successful quantitative comparison between experimental observations and first principles 2D full-wave simulations. The broadening of the beam has important implications for control of tokamak discharges through localized electron cyclotron deposition needed for eliminating magnetohydrodynamic instabilities. This new predictive capability is mandatory to design & operate present & future tokamaks in such a way that microwave heating schemes achieve their intended objectives.

Keywords: tokamaks, plasma heating, microwaves, plasma turbulence, simulations, experiments, microwave beam broadening

(Some figures may appear in colour only in the online journal)

* Author to whom any correspondence should be addressed.

The scattering of electromagnetic (EM) radiation by wavelength-sized inhomogeneities in the transmission medium is not fully understood: it is challenging to describe analytically except in a limited number of special cases and the tools of geometric optics cannot be applied since the assumptions on which they are based are not satisfied. Magnetized plasmas are interesting media for studying these phenomena: on the one hand, the refractive index can be reliably calculated (assuming background density, temperature and magnetic field are known). On the other hand magnetized plasmas exhibit exotic effects including birefringence and various polarization-dependent resonances and cut-offs. Some of the first observations of plasma waves were in the field of ionospheric physics; the underlying wave-plasma interactions remain relevant today for radio and satellite communication [1]. The effect of locally strong plasma density irregularities still provides a challenge in modeling EM wave propagation across the ionosphere [2].

Magnetic confinement fusion studies provide a variety of experiments well-equipped with diagnostics for studying the physics of EM wave propagation. Microwaves are used in tokamaks for diagnostic purposes such as measuring the plasma temperature via electron cyclotron emission and characterizing plasma turbulence via reflectometry and Doppler back-scattering [3]. Microwaves are also used in tokamaks for heating and current drive via the injection of a high power beam whose frequency is chosen to coincide with a particular resonance at the desired absorption location [4, 5]. ITER, the next generation tokamak currently under construction [6], will rely on high power microwave injection for heating the plasma in its core, for driving currents to control and mitigate magnetohydrodynamic instabilities, and to stabilize neoclassical tearing modes (NTMs) which are magnetic reconnection instabilities associated with the interplay of local reductions in plasma current and flattening of the pressure profile, reducing energy confinement of the device. Effective stabilization of the NTMs requires, however, precise spatial localization of the current driven by the microwaves [7–10]. In this letter, we demonstrate how turbulence in the tokamak plasma edge is responsible for substantial broadening of the injected heating beam by successful quantitative agreement between experimental measurements and first-principles simulations.

The present study is based on experimental observations and numerical simulations of the DIII-D tokamak plasma [11]: typical parameters are major radius $R = 1.7\,\mathrm{m}$, minor radius $a = 0.67\,\mathrm{m}$, plasma current $I_\mathrm{p} = 800\,\mathrm{kA}$ and on-axis toroidal magnetic field $B_\mathrm{t} = 2\,\mathrm{T}$. The facility's gyrotrons can deliver 3 MW of microwave power for heating and current drive including NTM stabilization [12, 13]. As shown in figure 1, the gyrotron beams are launched from a set of steerable mirrors located above the midplane on the tokamak's outboard side; their polarization and frequency ($f_0 = 110\,\mathrm{GHz}$, corresponding to a vacuum wavelength $\lambda_0 \approx 2.7\,\mathrm{mm}$) are optimized for second harmonic X-mode absorption at a magnetic field strength of 2 T. The plasma is optically thick at this resonance: the beam is totally absorbed. The beam waist radius at the launcher is approximately $65\,\mathrm{mm} \approx 24\,\lambda_0$, corresponding to a beam divergence of $\sim 1°$.

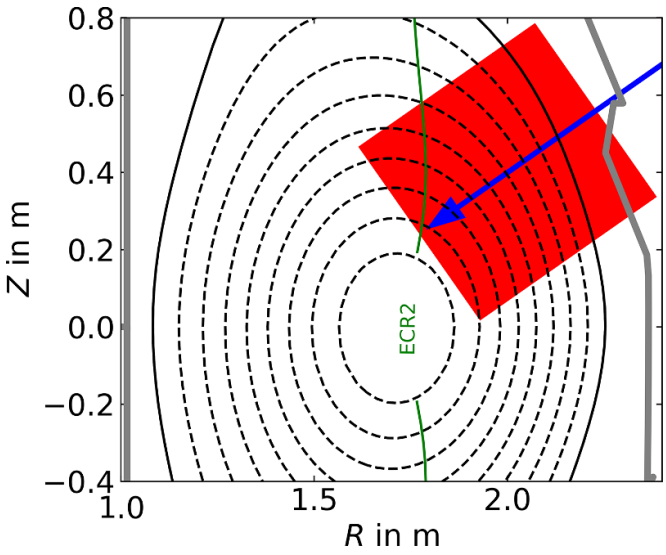

Figure 1. Cross-section of the DIII-D tokamak, dashed lines represent closed flux surfaces, the solid black line represents the separatrix, and the vacuum vessel is indicated by the thick grey line. The injected microwave beam is illustrated by the blue arrow, the resonant magnetic field strength by the green line, and the full-wave simulation domain by the red rectangle.

The NTMs are known to exist on rational surfaces where the ratio of poloidal to toroidal transits of the magnetic field is a rational number m/n with m and n small integers; typically the most unstable NTMs exist on the surfaces $(m,n) = (3,2)$ and $(2,1)$. The NTM mitigation strategy is therefore to target the beam at those surfaces. Broadening or misaligning the beam leads to wasted power (reduced machine efficiency) and might require additional modulation of the microwave power [14]. In the worst case it leads to failure to stabilize the NTM (and critical loss of plasma confinement).

The strategy for the present investigation has been first to deduce the deposition profile from measuring the heating profile. Due to transport during the finite time needed for the measurement, the width of the measured heating profile appears, as a rule, larger than the width of the illuminated region. The latter is hence to be inferred from a careful transport analysis, as detailed below. It is found that the power deposition is broadened substantially compared to what would be expected due to refractive effects of the background plasma density alone calculated using the ray tracing code TORAY-GA [15] (which accounts for the effects of the 1D plasma temperature and density profiles, but not for the effect of plasma density fluctuations). This is in agreement with similar observations reported from other experiments [16, 17]. We then performed a first-principles full-wave simulation of the heating beam's propagation through the experimentally-measured edge turbulence (using the full-wave code EMIT-2D, which is a novel version of EMIT-3D [18]). These measurements and simulations are compared for three distinct operation scenarios with varying shape of the equilibrium profiles and of the fluctuation degree showing very good agreement.

The microwave beam heat deposition profile is isolated from the resulting heat transport by power-modulating the

injected microwave beam with a square wave at 70 Hz in an otherwise stationary discharge: the absorption is highly localized and its modulation generates a time-periodic heat wave propagating away from the deposition layer. The modulation is sufficiently fast that the resulting density perturbation is negligible [19, 20]. The electron temperature can be measured using electron cyclotron emission (at the fundamental) with excellent temporal and spatial resolution of 2 μs and approximately 5 mm, respectively. The time variation of the temperature profile enables us to deduce the heat transport coefficients D and V, the diffusion and convection coefficients, respectively. A dedicated fitting analysis involving the energy transport equation including harmonics of the modulation frequency, outlined below and described in detail in [21, 22], yields the power deposition profile as a separate fitting parameter to the heat transport coefficients. We note that the time scale of the fastest harmonic used in the fitting analysis ($\approx$1.5 ms) is still an order of magnitude slower than the electron collision time.

Local conservation of energy is stated by

$$\frac{\partial}{\partial t}\left(\frac{3}{2}nT_\mathrm{e}\right)+\nabla\cdot\left(Q_\mathrm{e}+\frac{5}{2}T_\mathrm{e}\Gamma_\mathrm{e}\right)=P_\mathrm{ECH}+P_\mathrm{other}, \qquad (1)$$

where n denotes the number density, subscript 'e' refers to the electron species, T the temperature, Q the heat flux, Γ the particle flux, P_ECH the electron cyclotron heating power, and P_other incident power from other sources (e.g. Ohmic heating). Linearizing and retaining only those quantities oscillating at harmonics of the microwave heating modulation frequency (denoted with tildes), we obtain

$$\tilde{P}_\mathrm{ECH}=\frac{3}{2}n\frac{\partial\tilde{T}_\mathrm{e}}{\partial t}+\nabla\cdot\tilde{Q}_\mathrm{e}. \qquad (2)$$

The perturbed ohmic heating power $\tilde{P}_\mathrm{other}$ has been neglected after verifying by transport simulations that it contributes only marginally (below 2%). The perturbed electron temperature $\tilde{T}_\mathrm{e}$ as obtained from the electron cyclotron emission (ECE) diagnostics for various harmonics is shown in figure 2. We note the perturbed quantities in equation (2) are complex, containing both amplitude and phase information. If we were to neglect transport completely ($\tilde{Q}_\mathrm{e}=0$), we could use equation (2) to estimate the power deposition profiles directly. The profiles are, however, broader than predicted by ray-tracing calculations using TORAY-GA, also shown in figure 2. The increased broadening of the deposition profile can be due to the initially neglected transport processes, due to a broadening of the injected microwave beam or a combination of both. The correlation of the observed broadening of the microwave beam with measurements of edge density turbulence (see figure 3) motivated the hypothesis of a causal link between the two phenomena. Therefore, we need to solve the complete model in equation (2) to determine the best fit values for $\tilde{P}_\mathrm{ECH}$ and transport coefficients given the measured amplitudes and phases of $\tilde{T}_\mathrm{e}$ at all of its harmonics. Note that we calculated >99.5% absorption of the microwave and thus assume the same shape for the deposition profile and the microwave beam profile at the position of the resonance. This is justified by a geometrical argument:

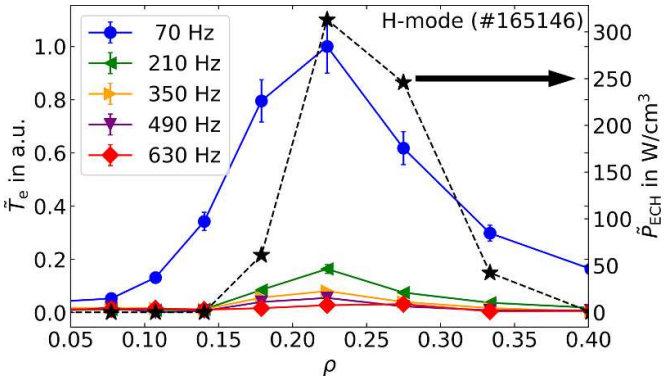

Figure 2. Amplitude perturbation of electron temperature $\tilde{T}_\mathrm{e}$ as obtained from the ECE diagnostic during power-modulated ECRH. Solid lines represent a guide to the eye to the data, dashed line indicates a guide to the eye to the deposition profile $\tilde{P}_\mathrm{ECH}$ obtained from the TORAY-GA code indicated by the filled black stars. The radial coordinate ρ denotes the normalized radius with $\rho=1$ corresponding to the last closed flux surface.

the absorption occurs at the 2nd harmonic X-mode resonance which, while broadened by thermal effects, is on the orders of a few centimeters thick. The beam size at the resonance is much larger, in small parts due to the divergence of the beam and mostly due to the additional broadening by turbulence (see this paper). Furthermore, given the relative position of launcher and target on the mostly vertical resonance layer and the nearly perpendicular launch of 110 GHz at 2 T in DIII-D (as illustrated in figure 1), the absorption layer thickness aligns along flux surfaces minimizing the impact of deposition width on beam size [23].

Employing a cylindrical large aspect ratio approximation, we integrate separately the real and imaginary parts of equation (2):

$$\tilde{Q}_\mathrm{e}(r,t)=\frac{1}{r}\int_0^r\left(\tilde{P}_\mathrm{ECH}-\frac{3}{2}n\frac{\partial\tilde{T}_\mathrm{e}}{\partial t}\right)r'\mathrm{d}r'. \qquad (3)$$

In a general form, the heat flux can be described by the sum of diffusive and convective parts. Linearizing the modulated heat flux by ordering terms based on their dependence on the predominant $\tilde{T}_\mathrm{e}$ perturbation [22] gives

$$\tilde{Q}_\mathrm{e}(r,t)=Dn\nabla\tilde{T}_\mathrm{e}+Vn\tilde{T}_\mathrm{e}+\tilde{\xi}, \qquad (4)$$

where $D(r)$ and $V(r)$ are the modulated diffusive and convective coefficients, respectively, and $\tilde{\xi}(r)$ represents coupled transport: these quantities are radially-varying and time-independent. Equating the right-hand sides of equations (3) and (4) and inserting the measured $\tilde{T}_\mathrm{e}(r)$ profiles gives us a set of equations (one for each harmonic's amplitude and phase) for $D(r)$, $V(r)$, $\tilde{\xi}(r)$ and $\tilde{P}_\mathrm{ECH}(r)$. Note that $\tilde{P}_\mathrm{ECH}$ and $\tilde{\xi}$ are both also functions of ω: $\tilde{P}_\mathrm{ECH}(r,\omega)$ is calculated from the calibrated ECH power measurements and $\tilde{\xi}(r,\omega)$ is estimated from a fit to previous perturbative transport studies [24]. The transport coefficients, D and V, can now be obtained from a best fit including the $\tilde{P}_\mathrm{ECH}(r)$ together with a value for $\tilde{\xi}$. The shape of the obtained radial profiles matches the expectations,

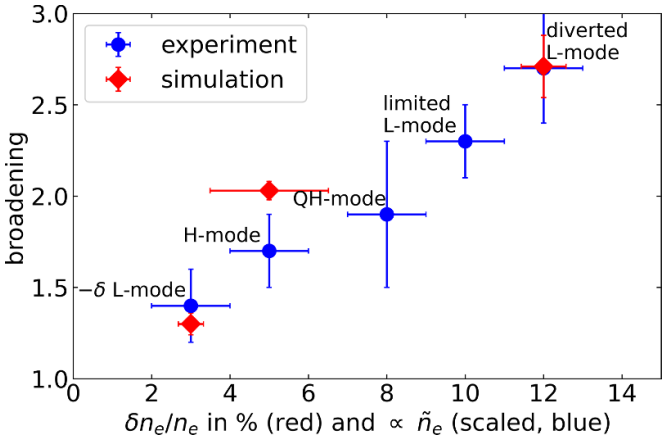

Figure 3. Beam broadening across a range of experimental scenarios, for which the fluctuation level at $\rho = 0.95$ is used as a label, deduced from experimental data and from full-wave simulations.

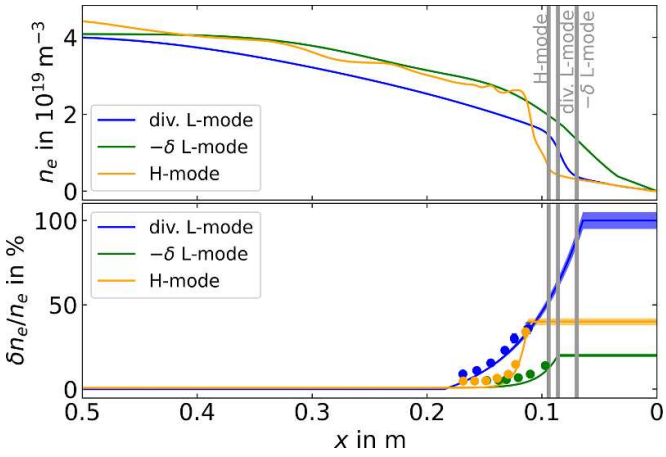

Figure 4. Radial electron density and fluctuation level profiles as used in the full-wave simulations. The radial coordinate corresponds to the full-wave grid, the positions of the separatrices are indicated by vertical grey lines. The n_e profiles shown correspond to a fit to Thomson scattering data normalized against a CO_2 interferometer and calibrated against the second harmonic X-mode density cutoff [35]. Symbols in the $\delta n_e/n_e$ profiles correspond to measurements from beam emission spectroscopy [36], solid lines correspond to the ensemble-averaged profiles used in the full-wave simulations.

e.g. the largest values of D were obtained for the L-mode scenarios, and ξ was found to contribute 20% at most [21, 22]. Microwave deposition profiles can be calculated and compared with the predicted profile by TORAY-GA yielding a broadening factor b (which we assume to be the same for the deposition profile and the microwave beam at the resonance layer, as explained above). Table 1 lists the broadening prior and after transport analysis. It is found that the deposition profile, i.e. the broadening after transport analysis, is up to three times the width predicted by ray tracing. A potential source of the broadening are plasma density fluctuations, as indicated by the experimental data in figure 3 which show the deduced beam broadening as a function of the fluctuation level at $\rho = 0.95$ obtained from five different plasma configurations (listed in table 1 in descending order of fluctuation level). A clear trend is seen, which motivates a full-wave simulation of the beam propagation. The error bars in the beam broadening are due to uncertainties from the measurements and from the fitting procedure [21].

At the plasma edge, turbulent density fluctuations are known to occur with fluctuation levels up to 100% [25]. Turbulence in magnetized plasmas is in general highly anisotropic with density structures that are elongated along the background magnetic field $\mathbf{B}_0$. Perpendicular to $\mathbf{B}_0$, the correlation length of the structures $L_\perp$ typically scales with the drift scale parameter $\rho_s = \sqrt{T_e m_i}/(eB_0)$ like $L_\perp \approx 5 - 10\rho_s$ [26]. The resulting structure size is with $L_\perp \approx 0.5\,\mathrm{cm}$ at the edge for a typical L-mode discharge [26] on the same order as the vacuum wavelength of the injected microwave, resulting in strong scattering [27]. The large fluctuation levels and structure size being similar to the vacuum wavelength λ_0 requires a full-wave treatment to correctly describe the scattering process. The broadening of an injected microwave beam due to plasma edge density fluctuations is an active field of research [14, 18, 27–33].

EMIT-2D [18] is a full-wave cold-plasma code (thus not accounting for absorption of the X-mode at the resonance layer) based on the finite-difference time-domain scheme. For the scenarios considered here, a novel 2D version of the code is used, as there is no need for computationally expensive 3D simulations to describe the scattering process (similar to the scenario discussed in [34], the beam propagates mostly perpendicular to the background magnetic field). The code enables us to simulate the propagation of EM waves with arbitrary background density and magnetic field. In the time-frame of the microwave, the plasma density fluctuations appear to be frozen due to their low velocity $\sim 10^4\,\mathrm{m\,s^{-1}}$ (as compared to the group velocity of the microwave). To account for the effect of turbulent density fluctuations on microwave propagation, an ensemble-average is made over a series of simulations. An initial ensemble of turbulence profiles for the diverted L-mode was created with the BOUT++ turbulence simulation code [37] using the Hermes model [38]. Experimentally-measured equilibrium profiles from DIII-D discharges were used as input parameters for the turbulence simulations as shown in figure 4. The obtained fluctuation levels correspond to those measured in the experiments, also shown in the figure. The BOUT++ simulations were only able to yield data close to the separatrix, whereas the absorption layer is located deep inside the plasma, see table 1. We have therefore used a synthetic turbulence generator [31, 34] to get profiles up to the absorption layer. The fluctuations are generated by a truncated sum of Fourier-like modes exhibiting a Gaussian k-spectrum. While usually power laws are found in the experiments [39], this is not expected to result in a noticeable difference in the beam broadening as the power laws and the Gaussian deviate significantly only at large k-values where strongly reduced broadening is expected [27]. As an input for the turbulence generator, equilibrium density profiles are required, which

Table 1. DIII-D discharge configurations with $B_t = 2\,\mathrm{T}$ for all shots. The physical units are MA for I_p, and $\bar{n}_e$ is in units of $10^{19}\,\mathrm{m}^{-3}$, b_1 and b_2 refer respectively to the broadening prior and after transport analysis (b_2 corresponds to the values plotted in figure 3).

Scenario	Shot	I_p	$\bar{n}_e$	κ	δ	ρ_{ECH}	b_1	b_2
diverted L-mode	165 078	1.0	2.9	1.8	0.45	0.3	3.5	2.7
limited L-mode	154 532	1.2	4.2	1.64	0.16	0.3	2.8	2.2
QH-mode	157 131	1.1	1.7	1.82	0.45	0.7	9.9	1.9
H-mode	165 146	1.0	3.2	1.83	0.32	0.25	2.3	1.7
$-\delta$ L-mode	166 192	0.9	3	1.32	−0.38	0.45	5.4	1.5

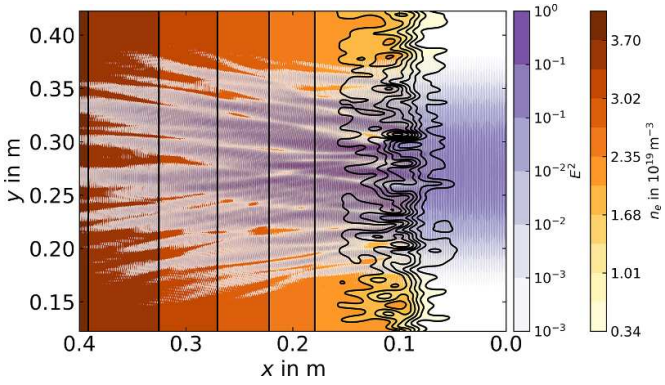

Figure 5. Snapshot of the absolute value of the wave electric field obtained from full-wave simulations together with the turbulent density profile for a diverted L-mode sample. The present figure is oriented such that going from right to left corresponds to decreasing ρ (see figure 1).

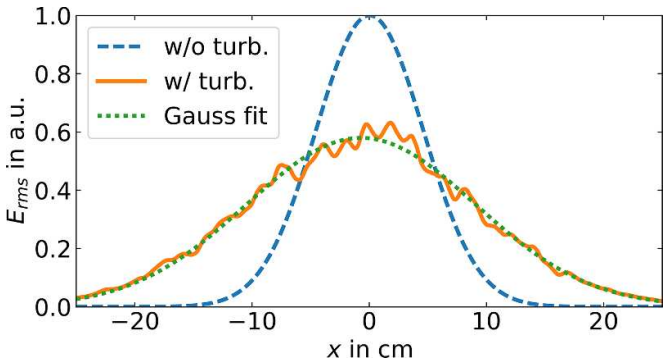

Figure 6. Transverse beam profile from the full-wave simulations taken at the end of the simulation plane. Shown are the reference case without turbulence, the ensemble-averaged signal for the diverted L-mode scenario and a Gaussian fit to the latter.

are obtained from Thomson scattering [35], and profiles of the fluctuation amplitude profiles. For the latter, exponential fits to the experimental data (obtained from beam emission spectroscopy [36]) were performed, truncated at a maximum value which was informed by the BOUT++ simulations and the literature [25, 40]. The perpendicular correlation length (the radial and vertical correlation lengths are assumed to be equal) used in the synthetic turbulence generator corresponds to a value of $L_\perp \approx 5\,\mathrm{mm}$, which is in agreement with previous experimental findings [41]. For the other scenario considered, the fluctuation amplitude profiles were chosen based on experimentally observed values [25, 39]. The fluctuation amplitude was set to a value of 0% in the core. Using a value of 1% had a negligible influence on the overall broadening of the microwave beam, in agreement with similar investigations [31]. The ensemble size was chosen to ensure convergence of the average, where a value of $N = 50$ was found to be sufficient.

Figure 5 shows as an example a snapshot of the wave electric field as obtained from the full-wave simulations together with the turbulent electron density for a diverted L-mode sample. The deteriorating effect of the fluctuations on the coherence of the microwave beam can be seen clearly, resulting in a splitting into multiple beams. Averaging over the ensemble of simulations, an effective broadening of the injected beam is observed. This is illustrated in figure 6 which shows the transverse beam profile at the end-plane of the simulation grid corresponding to the position of the absorption layer. The fluctuations result in a decrease of the central peak amplitude of the beam together with an increase of its width. The width of a fitted Gaussian can be compared with the reference case, resulting in a relative beam broadening of $w_{\mathrm{fluct}}/w_{\mathrm{no\text{-}fluct}} \approx 2.1$.

The resulting values of the broadening can now be directly compared with the values obtained from the ECE measurements. Figure 3 shows the relative beam broadening as a function of the relative fluctuation level at $\rho = 0.95$. The error bars in beam broadening are due to the statistical error of the ensemble average and the fluctuation level uncertainty is given by the radial uncertainty of the fluctuation level measurements to which the profiles used in the full-wave simulations are matched. The beam broadening deduced from the transport model applied to experiments and the broadening calculated by the full-wave simulations are consistent within the computed error bars across a wide range of fluctuation levels. A quadratic scaling with fluctuation level as observed, for example, in [27], is not expected here due to the strong variation in background density across the fluctuation layer and the more complicated shape of the fluctuation layer itself (which is in agreement with recent numerical investigations of beam broadening in realistic experimental scenarios [31]).

We have shown that edge turbulence can dramatically broaden the deposition profile of the microwave beam above what would be expected otherwise in DIII-D. For the first time, we have demonstrated experimentally the correlation between observed beam broadening and turbulent edge density fluctuations over a wide range of fluctuation levels. Very good quantitative agreement with first-principles 2D full-wave simulations has proven the direct causal link between these phenomena. This work has consequences for ITER: it confirms the wisdom of the vertical orientation of the NTM stabilization system, which minimizes the amplitude of the turbulent fluctuations through which the beam must propagate [31]. Moreover it validates a quantitatively-accurate predictive

simulation tool which can be used to calculate beam broadening and, if necessary, to formulate effective mitigation strategies.

The authors acknowledge access to the EUROfusion High Performance Computer (Marconi-Fusion) through EUROfusion, and to the HELIOS supercomputer system at Computational Simulation Centre of International Fusion Energy Research Centre (IFERC-CSC), Aomori, Japan, under the Broader Approach collaboration between Euratom and Japan, implemented by Fusion for Energy and JAEA. Some of this work has been carried out within the framework of the EUROfusion Consortium and has received funding from the Euratom research and training programme 2014–2018 under Grant Agreement No. 633053. The views and opinions expressed herein do not necessarily reflect those of the European Commission. This material is based upon work supported by the U.S. Department of Energy, Office of Science, Office of Fusion Energy Sciences, using the DIII-D National Fusion Facility, a DOE Office of Science user facility, under Award DE-FC02-04ER54698 and DE-FG03-97ER54415. DIII-D data shown in this paper can be obtained in digital format by following the links at https://fusion.gat.com/global/D3D_DMP One of the authors (MBT) was funded by the EPSRC Centre for Doctoral Training in Science and Technology of Fusion Energy Grant EP/L01663X. The authors thank Drs. Ben Dudson, David Dickinson and David Hatch for useful discussions. The authors are indebted to the efforts of the open-source software community.

ORCID iDs

M.W. Brookman https://orcid.org/0000-0002-5838-1630
L.A. Holland https://orcid.org/0000-0002-3867-1833
J.B. Leddy https://orcid.org/0000-0002-4492-7858
C.C. Petty https://orcid.org/0000-0003-4534-9073
T.L. Rhodes https://orcid.org/0000-0002-8311-4892
R.G.L. Vann https://orcid.org/0000-0002-3105-2546
A. Köhn-Seemann https://orcid.org/0000-0002-1192-2057

References

[1] Priyadarshi S. 2015 *Surv. Geophys.* **36** 295
[2] Strangeways H.J., Zernov N.N. and Gherm V.E. 2014 *Radio Sci.* **49** 899
[3] Hartfuss H.-J. and Geist T. 2014 *Fusion Plasma Diagnostics with Mm-Waves* (Weinheim: Wiley-VCH)
[4] Bornatici M., Cano R., De Barbieri O. and Engelmann F. 1983 *Nucl. Fusion* **23** 1153
[5] Erckmann V. and Gasparino U. 1994 *Plasma Phys. Control. Fusion* **36** 1869
[6] Shimada M. *et al* 2007 *Nucl. Fusion* **47** S1
[7] Zohm H. 1997 *Phys. Plasmas* **4** 3433
[8] Hegna C.C. and Callen J.D. 1997 *Phys. Plasmas* **4** 2940
[9] LaHaye R.J. *et al* 2006 *Phys. Plasmas* **13** 055501
[10] Sauter O., Henderson M.A., Ramponi G., Zohm H. and Zucca C. 2010 *Plasma Phys. Control. Fusion* **52** 025002
[11] Solomon W.M. (The DIII-D Team) 2017 *Nucl. Fusion* **57** 102018
[12] Lohr J. *et al* 2005 *Fusion Sci. Technol.* **48** 1226
[13] Kolemen E., Welander A.S., La Haye R.J., Eidietis N.W., Humphreys D.A., Lohr J., Noraky V., Penaflor B.G., Prater R. and Turco F. 2014 *Nucl. Fusion* **54** 073020
[14] Poli E. *et al* 2015 *Nucl. Fusion* **55** 013023
[15] Prater R. *et al* 2008 *Nucl. Fusion* **48** 035006
[16] Kirov K.K., Leuterer F., Pereverzev G.V., Ryter F. and Suttrop W. (ASDEX Upgrade team) 2002 *Plasma Phys. Control. Fusion* **44** 2583
[17] Leuterer F., Kirov K., Pereverzev G., Ryter F. and Wagner D. 2003 *Nucl. Fusion* **43** 744
[18] Williams T.R.N., Köhn A., O'Brien M.R. and Vann R.G.L. 2014 *Plasma Phys. Control. Fusion* **56** 075010
[19] Luce T.C. *et al* 2005 *32nd EPS Conf. on Plasma Phys. (Tarragona)* p -5.038
[20] Slief J.H., van Kampen R.J.R., Brookman M.W. and van Berkel M. 2022 *Phys. Plasmas* **29** 010703
[21] Brookman M.W., Austin M.E., Gentle K.W., Petty C.C., Ernst D.E., Peysson Y., Decker J. and Barada K. 2017 *EPJ Web Conf.* **147** 03001
[22] Brookman M.W. *et al* 2021 *Phys. Plasmas* **28** 042507
[23] Slief J.H., van Kampen R.J.R., Brookman M.W., van Dijk J., Westerhof E. and van Berkel M. 2023 *Nucl. Fusion* **63** 026029
[24] Fredrickson E.D., Austin M.E., Groebner R., Manickam J., Rice B., Schmidt G. and Snider R. 2000 *Phys. Plasmas* **7** 5051
[25] Zweben S.J., Boedo J.A., Grulke O., Hidalgo C., LaBombard B., Maqueda R.J., Scarin P. and Terry J.L. 2007 *Plasma Phys. Control. Fusion* **49** S1
[26] Rhodes T.L., Leboeuf J.-N., Sydora R.D., Groebner R.J., Doyle E.J., McKee G.R., Peebles W.A., Rettig C.L., Zeng L. and Wang G. 2002 *Phys. Plasmas* **9** 2131
[27] Köhn A., Holzhauer E., Leddy J., Thomas M.B. and Vann R.G.L. 2016 *Plasma Phys. Control. Fusion* **58** 105008
[28] Tsironis C., Peeters A.G., Isliker H., Strintzi D., Chatziantonaki I. and Vlahos L. 2009 *Phys. Plasmas* **16** 112510
[29] Sysoeva E.V., da Silva F., Gusakov E.Z., Heuraux S. and Popov A.Y. 2015 *Nucl. Fusion* **55** 033016
[30] Peysson Y., Decker J. and Morini L. 2012 *Plasma Phys. Control. Fusion* **54** 045003
[31] Snicker A., Poli E., Maj O., Guidi L., Köhn A., Weber H., Conway G., Henderson M. and Saibene G. 2018 *Nucl. Fusion* **58** 016002
[32] Chellaï O. *et al* 2018 *Phys. Rev. Lett.* **120** 105001

[33] Chellaï O., Alberti S., Furno I., Goodman T., Maj O., Merlo G., Poli E., Ricci P., Riva F. and Weber H. 2021 *Nucl. Fusion* **61** 066011
[34] Köhn A., Guidi L., Holzhauer E., Maj O., Poli E., Snicker A. and Weber H. 2018 *Plasma Phys. Control. Fusion* **60** 075006
[35] Carlstrom T.N. *et al* 1992 *Rev. Sci. Instrum.* **63** 4901
[36] McKee G., Ashley R., Durst R., Fonck R., Jakubowski M., Tritz K., Burrell K., Greenfield C. and Robinson J. 1999 *Rev. Sci. Instrum.* **70** 913
[37] Dudson B.D., Umansky M.V., Xu X.Q., Snyder P.B. and Wilson H.R. 2009 *Comput. Phys. Commun.* **180** 1467–80
[38] Dudson B.D. and Leddy J. 2017 *Plasma Phys. Control. Fusion* **59** 054010
[39] Conway G.D. 2008 *Plasma Phys. Control. Fusion* **50** 124026
[40] Rettig C.L., Peebles W.A., Burrell K.H., Doyle E.J., Groebner R.J., Luhmann J.N.C. and Philipona R. 1993 *Nucl. Fusion* **33** 643
[41] McKee G. *et al* 2001 *Nucl. Fusion* **41** 1235